

Delft University of Technology

CFD 3: LES Assignment 1

Delft University of Technology, Delft, South Holland, 2628 CD

Changkyu Park 4646061

Submission Date: March 29, 2021
Course: AE4139

Contents

1	Physical coordinates and Fourier wave numbers	2
2	Compressibility of the flow	2
3	Q-criterion	4
4	Box-averaged turbulence kinetic energy	6
5	Dissipation rate	6
6	3-D energy spectrum	6
7	Dissipation spectrum	6
8	Kolmogorov scaling	8
9	Reynolds numbers	8
10	Filtration of DNS solution for LES solution	9
11	Vorticity and velocity magnitude of DNS and LES solution	9
12	Subgrid scale (SGS) stress tensor	12
13	Smagorinsky's model	14
14	Galilei invariant Bardina model	16

1. Physical coordinates and Fourier wave numbers

The physical coordinates (x_i, y_j, z_k) of the cubic domain in all 3 dimensions consist of $N = 192$ points that are equally distributed over the range $[0, 2\pi(1 - 1/N)]$. Although the domain in a single dimension stretches until 2π , due to the periodic boundary condition, this location does not have a gridpoint. The equidistant spacing h is then

$$h = \frac{2\pi(1 - \frac{1}{N})}{N - 1}.$$

As for the Fourier wave numbers $(\xi_{x,i}, \xi_{y,j}, \xi_{z,k})$, they are:

$$0, 1, 2, \dots, \frac{N}{2} - 1, -\frac{N}{2}, -\frac{N}{2} + 1, \dots, -2, -1$$

in order. Hence, there are also 192 wave numbers.

2. Compressibility of the flow

To determine the compressibility of the flow, the divergence of the flow's velocity field, $\mathbf{u} = (u, v, w)$, is

$$\nabla \cdot \mathbf{u} = \frac{\partial u}{\partial x} + \frac{\partial v}{\partial y} + \frac{\partial w}{\partial z}$$

must be calculated. For the discretized domain, this is done by computing the root-mean-square (r.m.s.) divergence. The differentiation involved in determining the divergence will be done in 2 ways: spectral differentiation and second order finite difference scheme.

Starting with the spectral differentiation, it is done by differentiating

$$\mathbf{u}(\mathbf{x}) = \sum_{\xi} \hat{\mathbf{u}}(\xi) e^{i\xi \cdot \mathbf{x}},$$

which is the discrete Fourier series of the velocity field where ξ is

$$\xi = [\xi_x, \xi_y, \xi_z]^T,$$

and $e^{i\xi \cdot \mathbf{x}}$ is

$$e^{i\xi \cdot \mathbf{x}} = e^{i\xi_x x} e^{i\xi_y y} e^{i\xi_z z}.$$

As such, derivative of u with respect to x , for example, can simply be expressed as

$$\frac{\partial u}{\partial x} = \sum_{\xi_x} i\xi_x \hat{u}(\xi) e^{i\xi \cdot \mathbf{x}},$$

in which the matrices are multiplied term by term. Likewise, $\partial v / \partial y$ and $\partial w / \partial z$ are

$$\frac{\partial v}{\partial y} = \sum_{\xi_y} i\xi_y \hat{v}(\xi) e^{i\xi \cdot \mathbf{x}} \text{ and}$$

$$\frac{\partial w}{\partial z} = \sum_{\xi_z} i\xi_z \hat{w}(\xi) e^{i\xi \cdot \mathbf{x}}$$

respectively. The r.m.s. for the discrete velocity field can then be calculated as

$$(r.m.s.)_{SD} = \sqrt{\frac{1}{N^3} \sum_{ijk} \left[\left(\frac{\partial u}{\partial x} \right)_i + \left(\frac{\partial v}{\partial y} \right)_j + \left(\frac{\partial w}{\partial z} \right)_k \right]^2}.$$

Using Parseval's theorem, this equation can be expressed as

$$(r.m.s.)_{SD} = \sqrt{\sum_{\xi} (i\xi_x \hat{u}(\xi) e^{i\xi \cdot \mathbf{x}} + i\xi_y \hat{v}(\xi) e^{i\xi \cdot \mathbf{x}} + i\xi_z \hat{w}(\xi) e^{i\xi \cdot \mathbf{x}})^2},$$

and the value was found to be

$$(r.m.s)_{SD} = 6.7553 \times 10^{-16}$$

$$(r.m.s)_{SD} = 0.$$

Thus, using spectral differentiation, it can be observed that the flow is incompressible since the divergence of the flow velocity is 0.

As for the finite difference scheme, central differencing scheme that is second order accurate is chosen. Unlike spectral differentiation that was executed in the spectral space, the finite difference scheme is done in physical space. The derivative of u with respect to x for an i -th node in the x -direction can then be expressed as

$$\left(\frac{\partial u}{\partial x}\right)_i = \frac{u_{i+1} - u_{i-1}}{2h}.$$

As such the full derivative can be written as

$$\frac{\partial u}{\partial x} = \sum_i \frac{u_{i+1} - u_{i-1}}{2h}.$$

Similarly, $\partial v/\partial y$ and $\partial w/\partial z$ are

$$\frac{\partial v}{\partial y} = \sum_j \frac{v_{j+1} - v_{j-1}}{2h} \quad \text{and}$$

$$\frac{\partial w}{\partial z} = \sum_k \frac{w_{k+1} - w_{k-1}}{2h}$$

respectively. In order to compute each of the derivatives, systems of equations must be set up. For example, for $\partial u/\partial x$, the system of equation is

$$\frac{\partial u}{\partial x} = A_{3D,x} u_{1D},$$

where $A_{3D,x}$ is of size $(N \times N \times N, N \times N \times N)$ and is built using 1-D sparse divergence matrix A_{1D} which consists of only +1 and -1 according to the central differencing scheme and u_{1D} is the 1-D vector of size $(N \times N \times N, 1)$ that is unpacked from u of size (N, N, N) . For each set of N components in each dimension, an $(N \times N)$ sparse matrix A_{1D} is set up and is visualised in Figure 1 for a smaller domain of $N = 10$ for clarity.

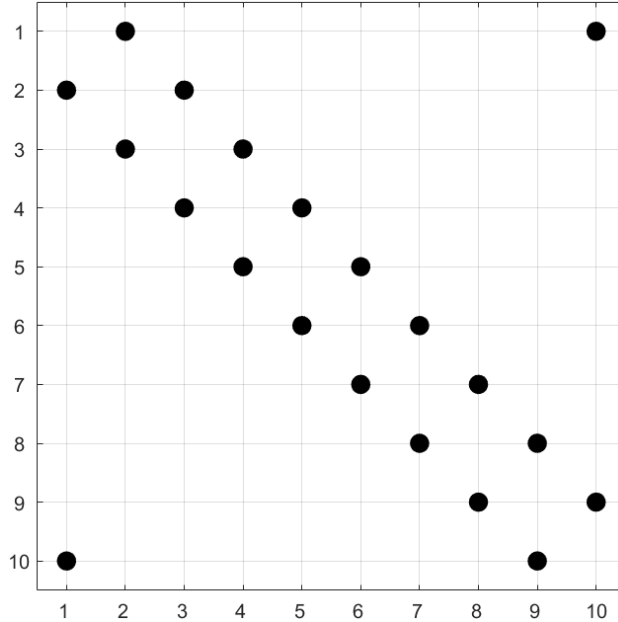


Fig. 1 Sparsity pattern of divergence matrix A_{1D} for $N = 10$

The implementation of the periodic boundary condition can be observed from the first and the last row whereby the 0-th node boundary is wrapped around and is replaced by the N -th node. Similarly, the $(N + 1)$ -th node, which represents the location at 2π , is replaced by the first node.

The 3-D divergence matrices can then be expressed as

$$\begin{aligned} A_{3D,x} &= I \otimes I \otimes A_{1D}, \\ A_{3D,y} &= I \otimes A_{1D} \otimes I \text{ and} \\ A_{3D,z} &= A_{1D} \otimes I \otimes I, \end{aligned}$$

where I is an identity matrix of size (N, N) and \otimes represents the Kronecker product.

The r.m.s. divergence is then calculated as

$$(r.m.s)_{FD} = \sqrt{\frac{1}{N^3} \left(\frac{\partial u}{\partial x} + \frac{\partial v}{\partial y} + \frac{\partial w}{\partial z} \right)^2}$$

$(r.m.s)_{FD} = 2.4872$

which is not 0 as it was observed for the spectral differentiation. This difference comes from the property of central differencing scheme which only uses the 2 neighbouring points to obtain local nodal information. On the other hand for spectral differentiation, it utilises all the discrete nodes to evaluate the derivative at a single node. Thus, the central differencing scheme introduces a lot more inaccuracy as it is limited in terms of the information it can see and use for a single grid point.

3. Q-criterion

The Q-criterion is expressed as

$$Q = -\frac{1}{2} \frac{\partial u_i}{\partial x_j} \frac{\partial u_j}{\partial x_i},$$

where the derivatives are evaluated in spectral space and the products between the derivatives are done in physical space. The 3-D iso-surfaces of the computed Q were visualised for 2 different iso- Q values. The first iso-surface shown in Figure 2 represents vortex surfaces with an iso- Q value of 2000. In the following Figure 3, vortex surfaces with iso- Q values of 1800 and 2000 are shown. It was observed that with decreasing iso- Q value, the domain gets denser with the vortex surfaces. Furthermore, it can be seen from Figure 3 that the vortex surfaces of the lower iso- Q value of 1800 overshadow the higher iso- Q of 2000 thus it is also realised that with decreasing iso- Q value, the vortex surfaces moves outwards in each of their respective position.

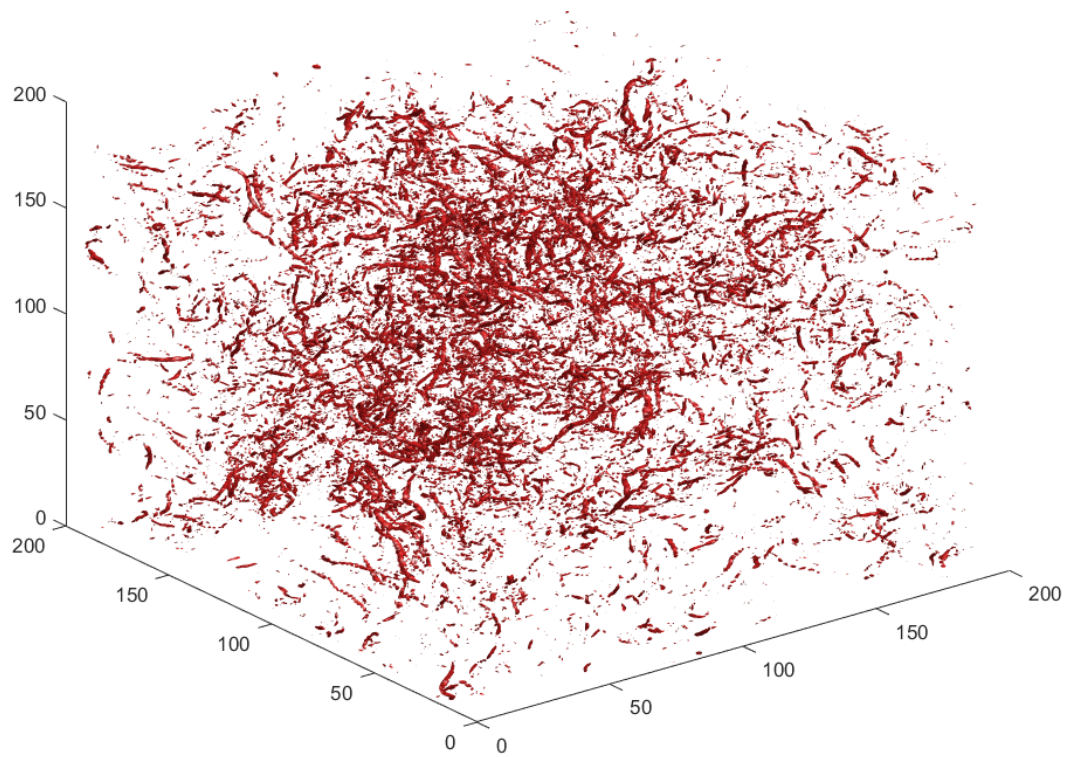


Fig. 2 Iso-surface plot of iso-Q = 2000

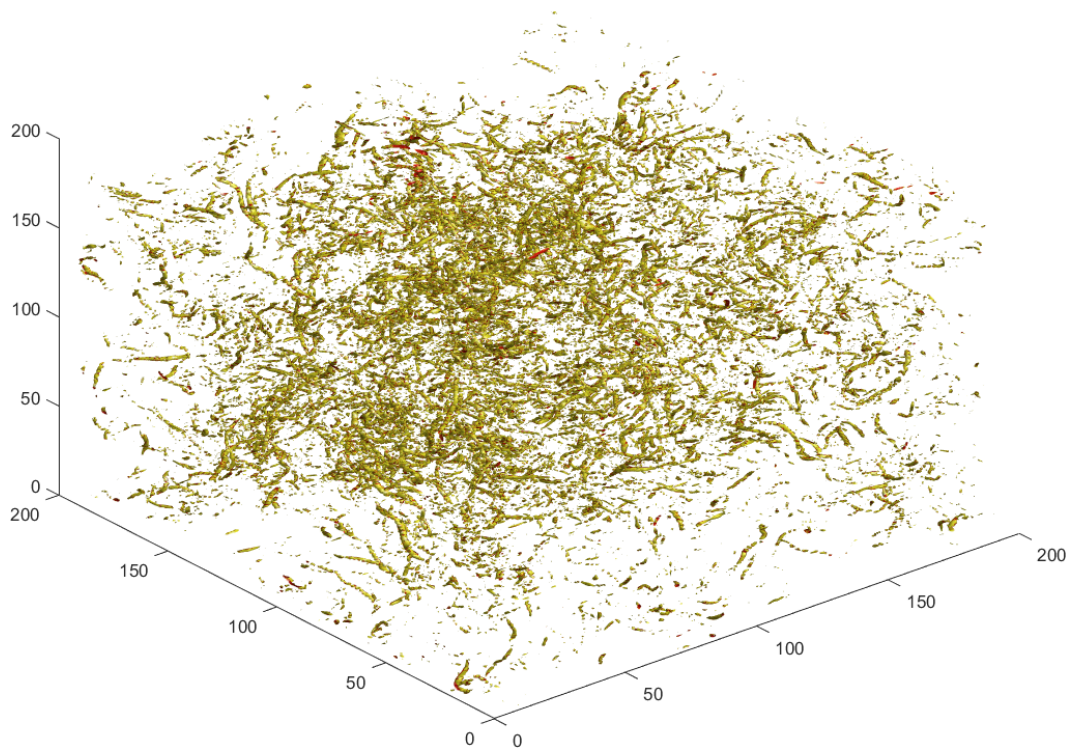


Fig. 3 Iso-surface plot of iso-Q = 1800 (yellow) and 2000 (red)

4. Box-averaged turbulence kinetic energy

The box-averaged turbulence kinetic energy in physical space can be expressed as

$$k_{phy} = \frac{1}{N^3} \sum_{ijk} \left[\frac{1}{2} \mathbf{u}(x_i, y_j, z_k) \cdot \mathbf{u}(x_i, y_j, z_k) \right].$$

The value was found to be

$$k_{phy} = 2.5061.$$

In the spectral space, it could be calculated using

$$k_{sp} = \sum_{\xi} \frac{1}{2} \hat{\mathbf{u}}(\xi) \cdot \hat{\mathbf{u}}^*(\xi)$$

and the value was found to be

$$k_{sp} = 2.5061.$$

Thus, the turbulence kinetic energy is said to be preserved in both physical and spectral space.

5. Dissipation rate

The dissipation rate is expressed as

$$\varepsilon = \nu \sum_{\xi} \xi^2 \hat{\mathbf{u}}(\xi) \cdot \hat{\mathbf{u}}^*(\xi),$$

where ν is the kinematic viscosity with a given value of 0.0008 and $*$ represents the complex conjugate. The value was found to be

$$\varepsilon = 0.8448.$$

6. 3-D energy spectrum

For the 3-D energy spectrum computation, the wave-number space is projected onto the integer wave numbers $\xi_n = \xi_0 n$ with $n \in \mathbb{N}$ and $\xi_0 = 2\pi/\mathcal{L}$. Since $\mathcal{L} = 2\pi$, $\xi_0 = 1$ and $\xi_n = n$. Thus, the integer wave numbers are

$$\xi_n = 1, 2, 3, \dots$$

The 3-D kinetic energy density spectrum can then be expressed as

$$E(\xi_n = \xi_0 n) = \sum_{\xi_0(n-\frac{1}{2}) \leq |\xi| < \xi_0(n+\frac{1}{2})} \frac{1}{2} \hat{\mathbf{u}}(\xi) \cdot \hat{\mathbf{u}}^*(\xi), \quad (6.1)$$

which represents spherical shells around each wave number magnitude where $|\xi|$ represents the wave number magnitudes and they are

$$|\xi|_{ijk} = \left(\xi_{x,i}^2 + \xi_{y,j}^2 + \xi_{z,k}^2 \right)^{1/2}.$$

The result of (6.1) has been plotted on double-logarithmic axes and is shown in Figure 4.

The turbulent energy cascade can be observed from the plot that features a small range of large scales, extensive inertial range and small scales.

7. Dissipation spectrum

The 3-D dissipation spectrum can then be expressed as

$$D(\xi_n) = 2\nu \xi_n^2 E(\xi_n)$$

and it is plotted in Figure 5 on a double-logarithmic axes as well.

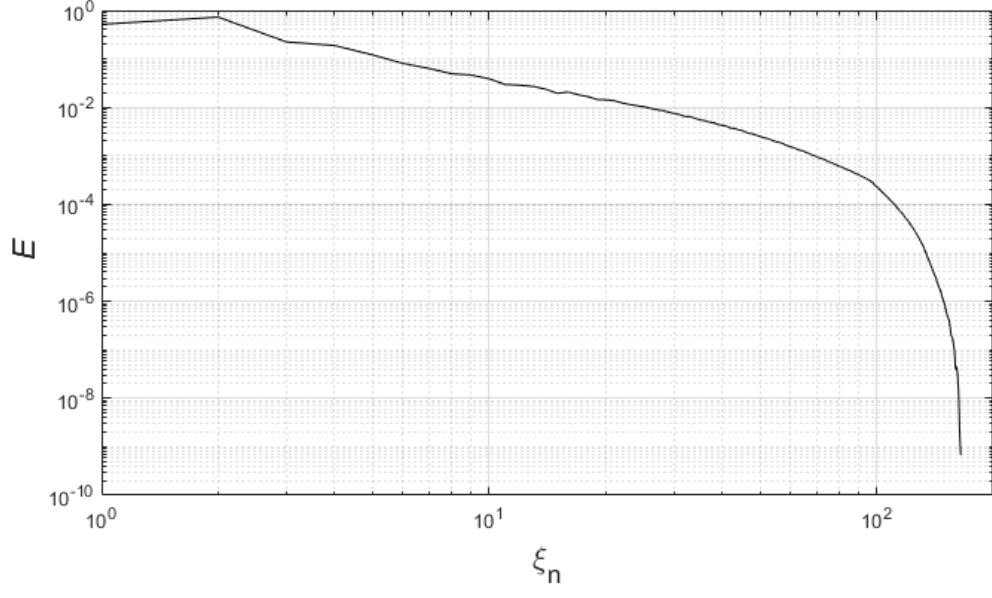


Fig. 4 3-D energy spectrum

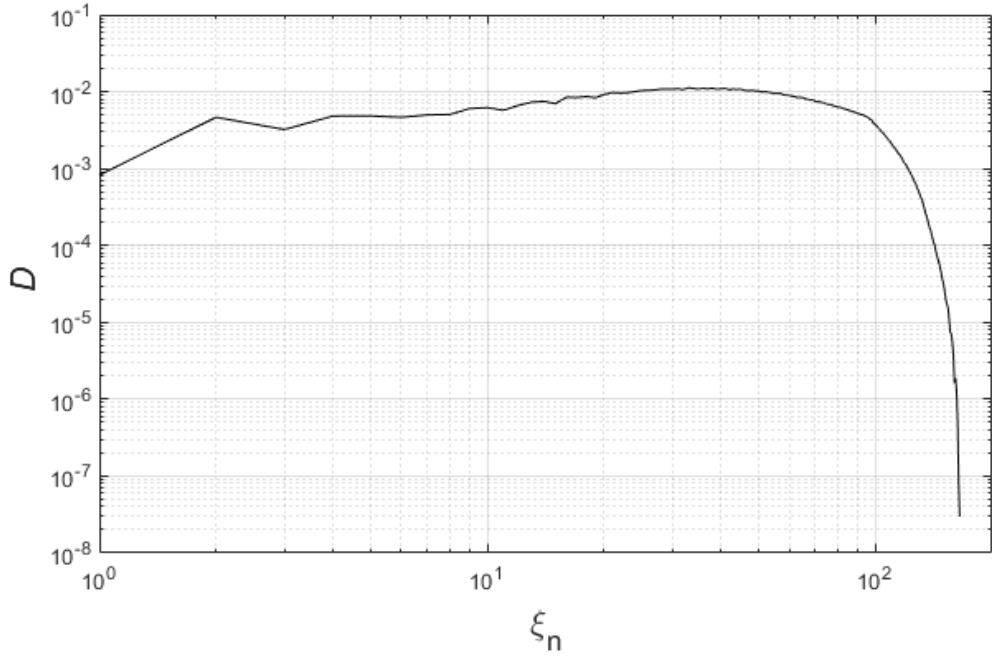


Fig. 5 3-D dissipation spectrum

The box averaged kinetic energy and dissipation rate were then computed from the 3-D spectrum using

$$k = \sum_n E(\xi_n) \text{ and}$$

$$\varepsilon = \sum_n D(\xi_n)$$

respectively. The values were then found to be

$$k_{3D} = 2.5061 \quad \text{and} \\ \varepsilon_{3D} = 0.8422.$$

Thus, it is realised that the turbulent kinetic energy can be exactly presented in the 3-D spectrum whereas for the dissipation rate, there is a small but acceptable difference due to approximation made for the spherical shell concept in (6.1) which leads to loss of information.

8. Kolmogorov scaling

The value of the Kolmogorov constant C_k was calculated using

$$\tilde{C}(\xi) = E(\xi)\varepsilon^{-2/3}\xi^{5/3}$$

based on Kolmogorov's $\xi^{-5/3}$ law and the mean of \tilde{C} values was taken. The slope of $-5/3$ was plotted together with Figure 4 to determine the range in which the inertial range lives and it is shown in Figure 6.

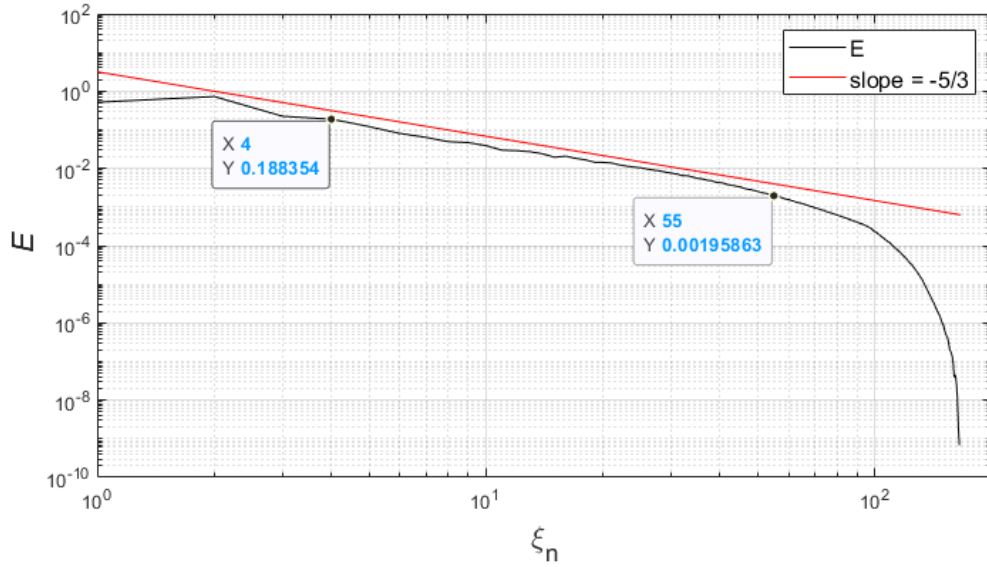


Fig. 6 3-D energy spectrum with a slope of $-5/3$

It could be observed that the inertial range was from $\xi_n = 4$ until $\xi_n = 55$. This range of values resulted in the Kolmogorov constant of

$$C_k = 2.1674,$$

which is significantly higher than the typical value of 1.5.

9. Reynolds numbers

The Reynolds number which characterises the large scales is

$$Re_L = \frac{k^2}{\varepsilon\nu},$$

where k is the turbulence kinetic energy. This Reynolds number was calculated and found to be

$$Re_L = 92929.$$

The corresponding integral length scale according to [1] is

$$L = \frac{k^{3/2}}{\varepsilon}$$

which gives a value of

$$L = 4.6961.$$

On the other hand, the Taylor micro-scale is expressed as

$$\lambda_g = \sqrt{\frac{10\nu k}{\varepsilon}},$$

giving a value of

$$\lambda_g = 0.1541. \quad (9.1)$$

The corresponding Reynolds number of the small scales is

$$Re_\lambda = \frac{\lambda_g \sqrt{\frac{2}{3}k}}{\nu}.$$

Using the value of λ_g obtained in (9.1), Reynolds number of the small scales is

$$Re_\lambda = 248.90.$$

10. Filtration of DNS solution for LES solution

The DNS solution was then filtered to a typical LES resolution of $N_{LES} \times N_{LES} \times N_{LES}$ with $N_{LES} = 24$ grid points. The corresponding filter width is

$$\begin{aligned} \Delta_{LES} &= \frac{2\pi(1 - \frac{1}{N_{LES}})}{N_{LES} - 1} \\ &= 0.2618, \end{aligned}$$

where the numerator represents the domain range. Its corresponding Nyquist wavenumber was then found to be

$$\begin{aligned} \xi_N &= \frac{\pi}{\Delta_{LES}} \\ \xi_N &= 12. \end{aligned}$$

The filter operation was then performed in spectral space on $\hat{\mathbf{u}}(\xi)$ using the top-hat filter. The spectral transfer function is

$$\hat{G}(|\xi|) = \frac{2\xi_N}{\pi|\xi|} \sin \frac{\pi|\xi|}{2\xi_N}.$$

Furthermore, \hat{G} was set to 0 for $|\xi| > \xi_N$. The energy and dissipation spectrum of the filtered LES solution was then plotted alongside the unfiltered DNS solution as shown in Figure 7 and Figure 8 respectively.

It can be seen in both figures that the cut-off wavenumber is $\xi_n = 12$. Moreover, the spectra for the LES solution increasingly deviates from the DNS solution as the wave number approaches $\xi_n = 12$. This is due to reduction in energy contribution from the upper range ($|\xi| < \xi(n + 1/2)|$) of (6.1) due to the filtration.

11. Vorticity and velocity magnitude of DNS and LES solution

The vorticity $\omega_z(\mathbf{x})$ is expressed as

$$\omega_z(\mathbf{x}) = \frac{\partial v}{\partial x} - \frac{\partial u}{\partial y}$$

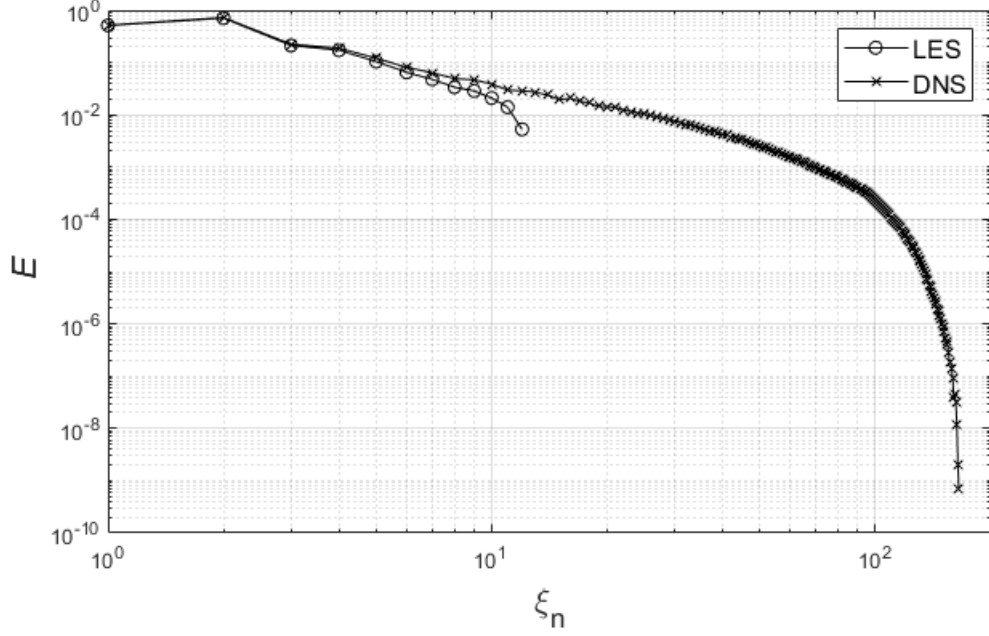


Fig. 7 Comparison of energy spectrum between DNS and LES solution

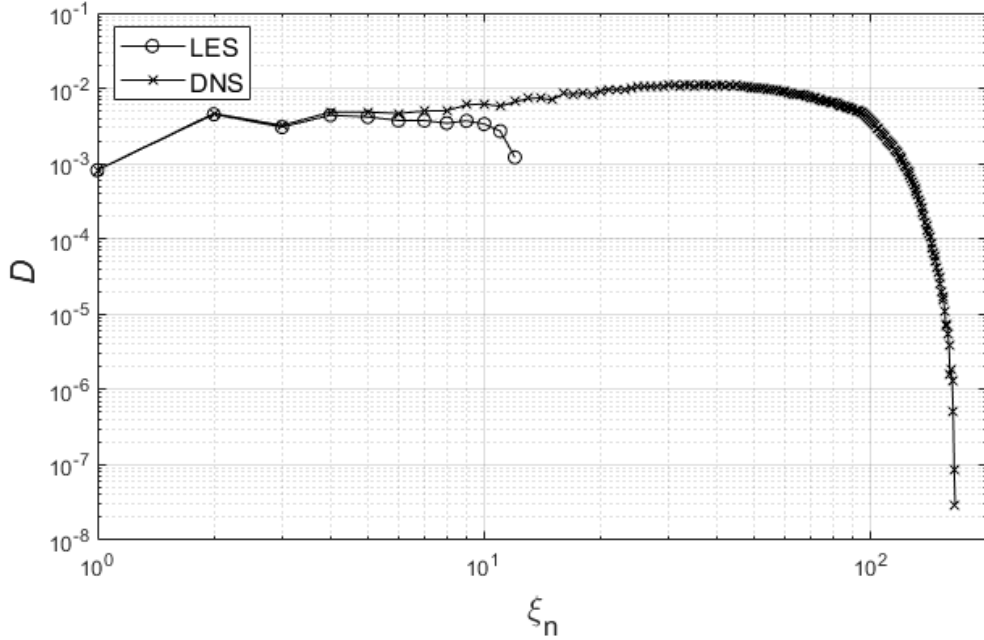


Fig. 8 Comparison of dissipation spectrum between DNS and LES solution

and the result for DNS and filtered LES solution are plotted and shown in Figure 9 and Figure 10 respectively on $x - y$ plane at $z \approx \pi$.

Firstly, it can be observed that the vorticity of the DNS solution has a much larger range of magnitudes, going from -150 to 150 approximately whereas it goes from -20 to 15 approximately for vorticity of the LES solution. Secondly, DNS solution features vorticities of much small length scales compared to LES solution which has filtered out these small scales and features only the larger length scales. Thus, this shows that the vorticities of smaller length scales that have been filtered out possess larger magnitudes.

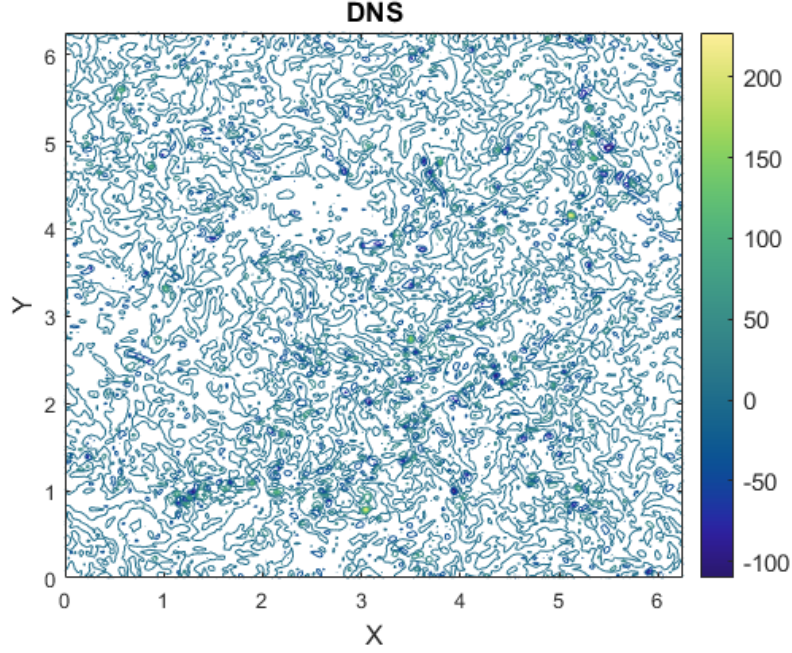


Fig. 9 Vorticity $\omega_z(\mathbf{x})$ of DNS solution on $x - y$ plane at $z \approx \pi$

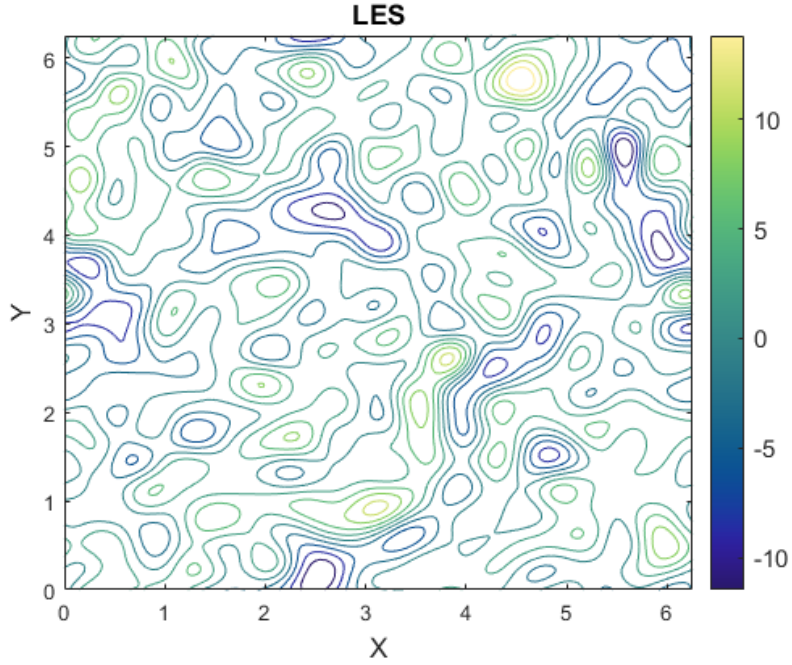


Fig. 10 Vorticity $\omega_z(\mathbf{x})$ of LES solution on $x - y$ plane at $z \approx \pi$

The velocity magnitude $\omega_z(\mathbf{x})$ of the DNS and filtered LES solution are plotted and shown in Figure 11 and Figure 12 respectively on $x - y$ plane at $z \approx \pi$ as well. It can be observed that the velocity magnitude of DNS features much more distinction between the different magnitudes whereas, for LES, this distinction is smoothed out and is seen blurry. Moreover, it can also be seen that velocities of lower magnitudes have been filtered out as the LES solution portrays a lot more high magnitude regions compared to the DNS solution.

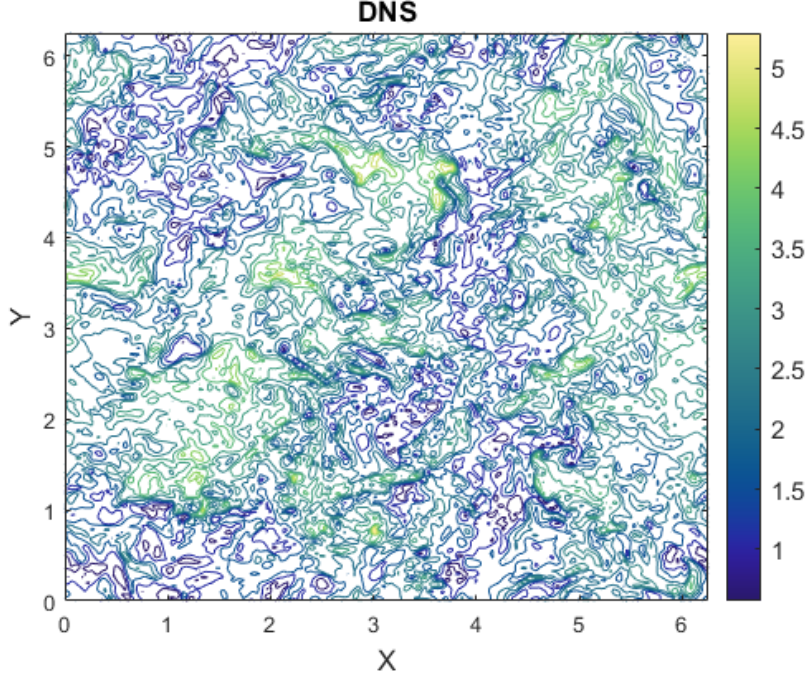


Fig. 11 Velocity magnitude $|u(x)|$ of DNS solution on $x - y$ plane at $z \approx \pi$

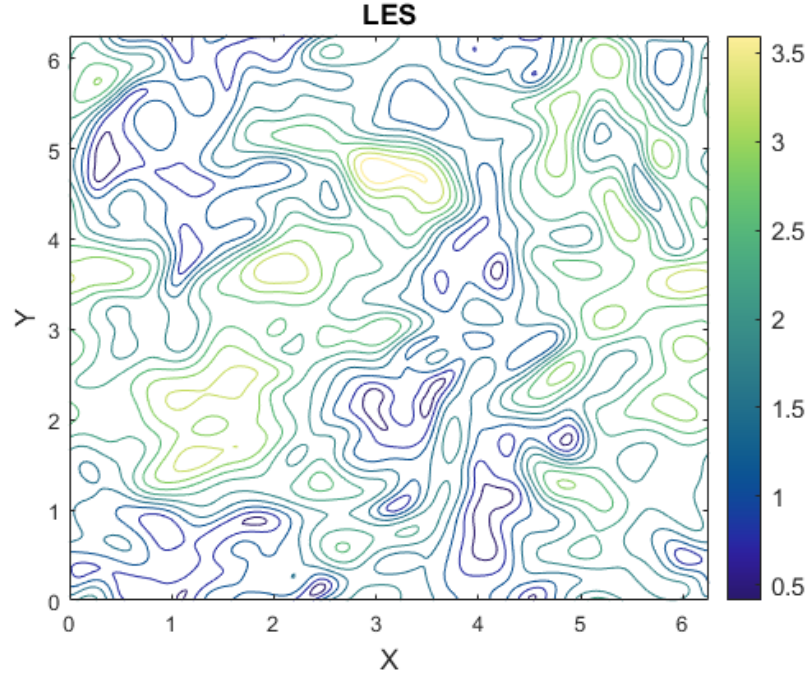


Fig. 12 Velocity magnitude $|u(x)|$ of LES solution on $x - y$ plane at $z \approx \pi$

12. Subgrid scale (SGS) stress tensor

The SGS stress tensor is expressed as

$$\tau_{ij} = \overline{u_i u_j} - \bar{u}_i \bar{u}_j$$

and its six independent components have been plotted in Figure 13 on $x - y$ plane at $z \approx \pi$ as well.

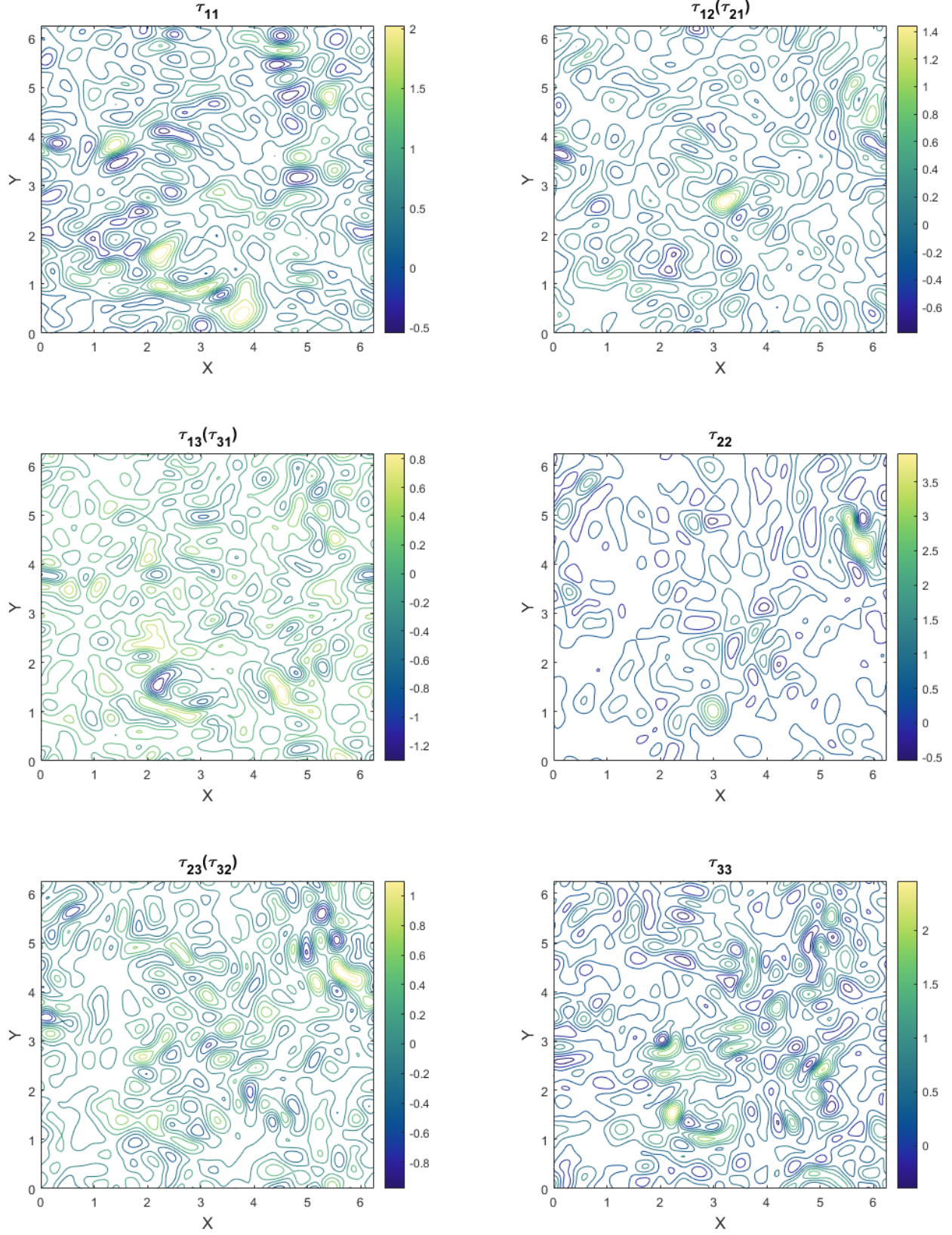


Fig. 13 Exact SGS stress tensor τ_{ij} on $x-y$ plane at $z \approx \pi$

Additionally, $C_s = 1.7$ was chosen due to the isotropic nature of vortices in the given domain as shown in iso-Q plots of Figure 2 and Figure 3.

13. Smagorinsky's model

The eddy viscosity of Smagorinsky's model is expressed as

$$\nu_{SGS} = (C_s \Delta)^2 \sqrt{2\bar{S}_{ij}\bar{S}_{ij}}$$

where C_s is the Smagorinsky constant, Δ is the filter width which is taken as Δ_{LES} and \bar{S}_{ij} is

$$\bar{S}_{ij} = \frac{1}{2} \left(\frac{\partial \bar{u}_i}{\partial x_j} + \frac{\partial \bar{u}_j}{\partial x_i} \right).$$

The Smagorinsky's eddy viscosity is shown in Figure 14.

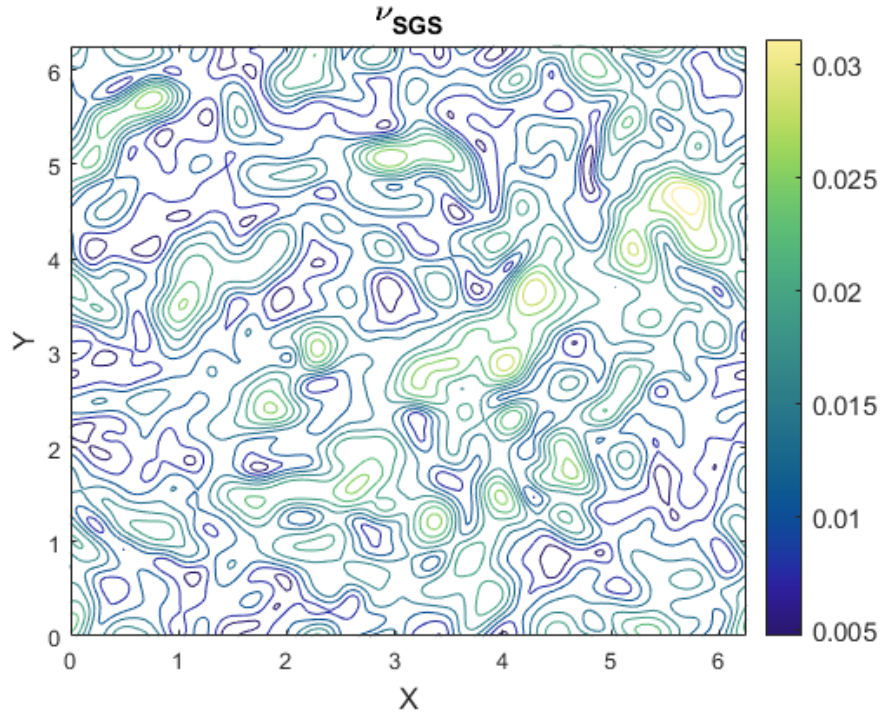


Fig. 14 Smagorinsky's eddy viscosity ν_{SGS} for $C_s = 0.17$ on $x - y$ plane at $z \approx \pi$

The SGS stress tensor of the Smagorinsky's model can be expressed as

$$\tau_{ij} = \frac{1}{3} \tau_{kk} \delta_{ij} - 2\nu_{SGS} \bar{S}_{ij}$$

whereby the first term can be ignored and only the second term is modelled. Thus, it ultimately is

$$\tau_{ij} = -2\nu_{SGS} \bar{S}_{ij}.$$

The six independent components of this SGS stress tensor of Smagorinsky's model have also been plotted on the $x - y$ plane at $z \approx \pi$ as shown in Figure 15.

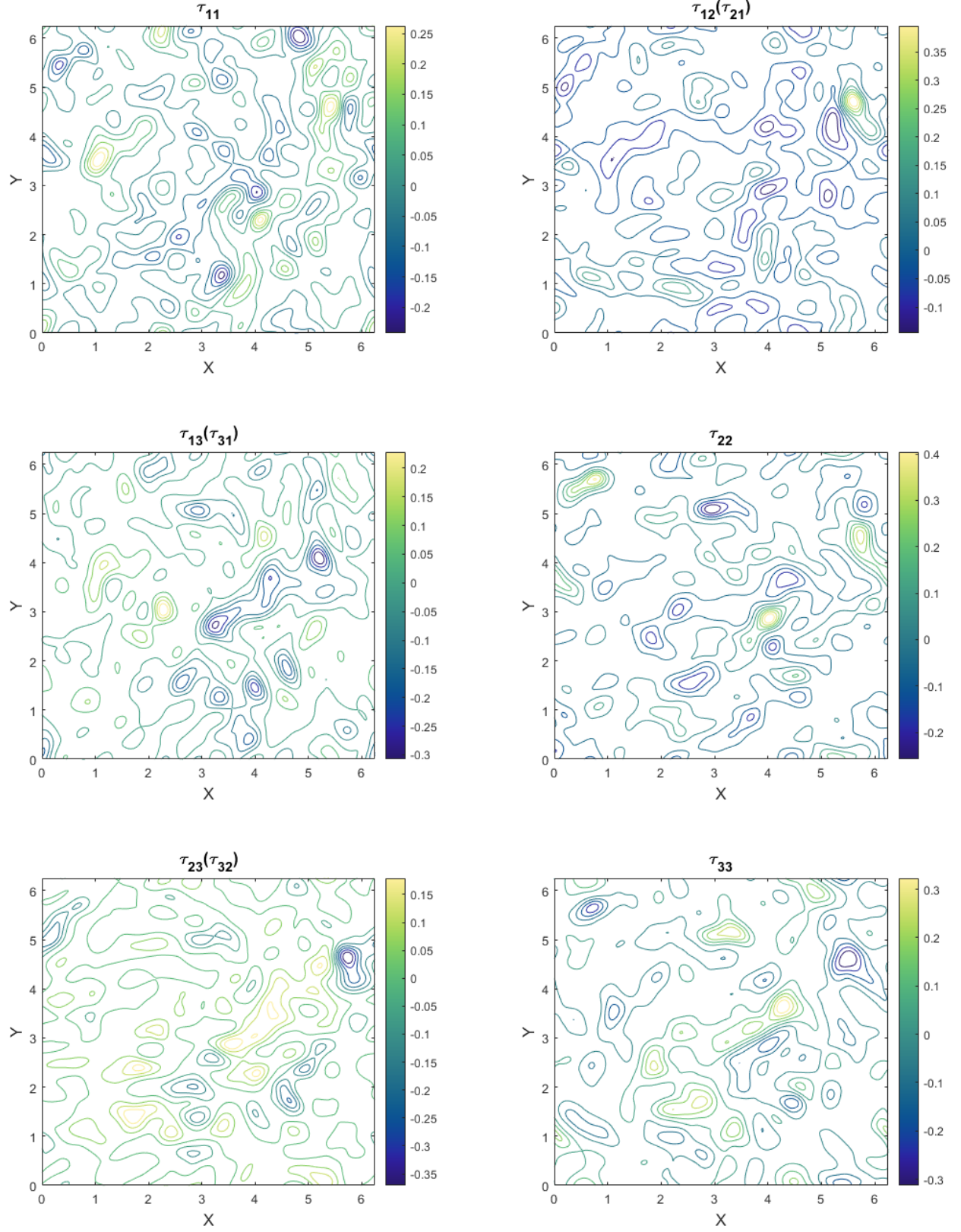


Fig. 15 Smagorinsky's SGS stress tensor τ_{ij} on $x-y$ plane at $z \approx \pi$

It is observed that Smagorinsky's SGS stress tensor has little agreement with the exact SGS stress tensor. In general, it looks as though there is no similarity at all with most of the characteristics in the plot of exact SGS stress being lost. Not only are the characteristic shapes lost but also the range of magnitudes of the stress tensor which are much smaller than that of the exact ones.

14. Galilei invariant Bardina model

For the Galilei invariant Bardina model, it is assumed that

$$\overline{ab} \approx \bar{a}\bar{b}$$

for arbitrary a and b . Thus, using the relation $\overline{u_i''} = \bar{u}_i - \bar{\bar{u}}_i$, the Reynolds and cross stresses are modelled as

$$\begin{aligned} R_{ij} &= \overline{u_i'' u_j''} \approx (\bar{u}_i - \bar{\bar{u}}_i) (\bar{u}_j - \bar{\bar{u}}_j) \\ C_{ij} &= \overline{\bar{u}_i u_j''} + \overline{u_i'' \bar{u}_j} \approx \bar{\bar{u}}_i (\bar{u}_j - \bar{\bar{u}}_j) + (\bar{u}_i - \bar{\bar{u}}_i) \bar{\bar{u}}_j \end{aligned}$$

respectively. The sum of Reynolds and cross stresses is known as Scale Similarity Model and it is expressed as

$$C_{ij} + R_{ij} \approx M_{ij} = C_B (\bar{u}_i \bar{u}_j - \bar{\bar{u}}_i \bar{\bar{u}}_j)$$

where C_B is a model constant. Taking note that the exact Leonard stress is

$$L_{ij} = \bar{\bar{u}}_i \bar{u}_j - \bar{u}_i \bar{\bar{u}}_j$$

and assuming $C_B = 1$, Bardina's SGS stress tensor can be expressed as

$$\begin{aligned} \tau_{ij} &= L_{ij} + R_{ij} + C_{ij} \\ &= \bar{\bar{u}}_i \bar{u}_j - \bar{u}_i \bar{\bar{u}}_j + \bar{u}_i \bar{u}_j - \bar{\bar{u}}_i \bar{\bar{u}}_j \\ &= \bar{\bar{u}}_i \bar{u}_j - \bar{\bar{u}}_i \bar{\bar{u}}_j. \end{aligned}$$

This was then plotted on $x - y$ plane at $z \approx \pi$ as shown in Figure 16. Unlike Smagorinsky's SGS stress tensor, Bardina's SGS stress tensor shows a large degree of similarity with the exact SGS stress tensor. However, the magnitudes of the stress tensor have also been reduced compared to the exact ones.

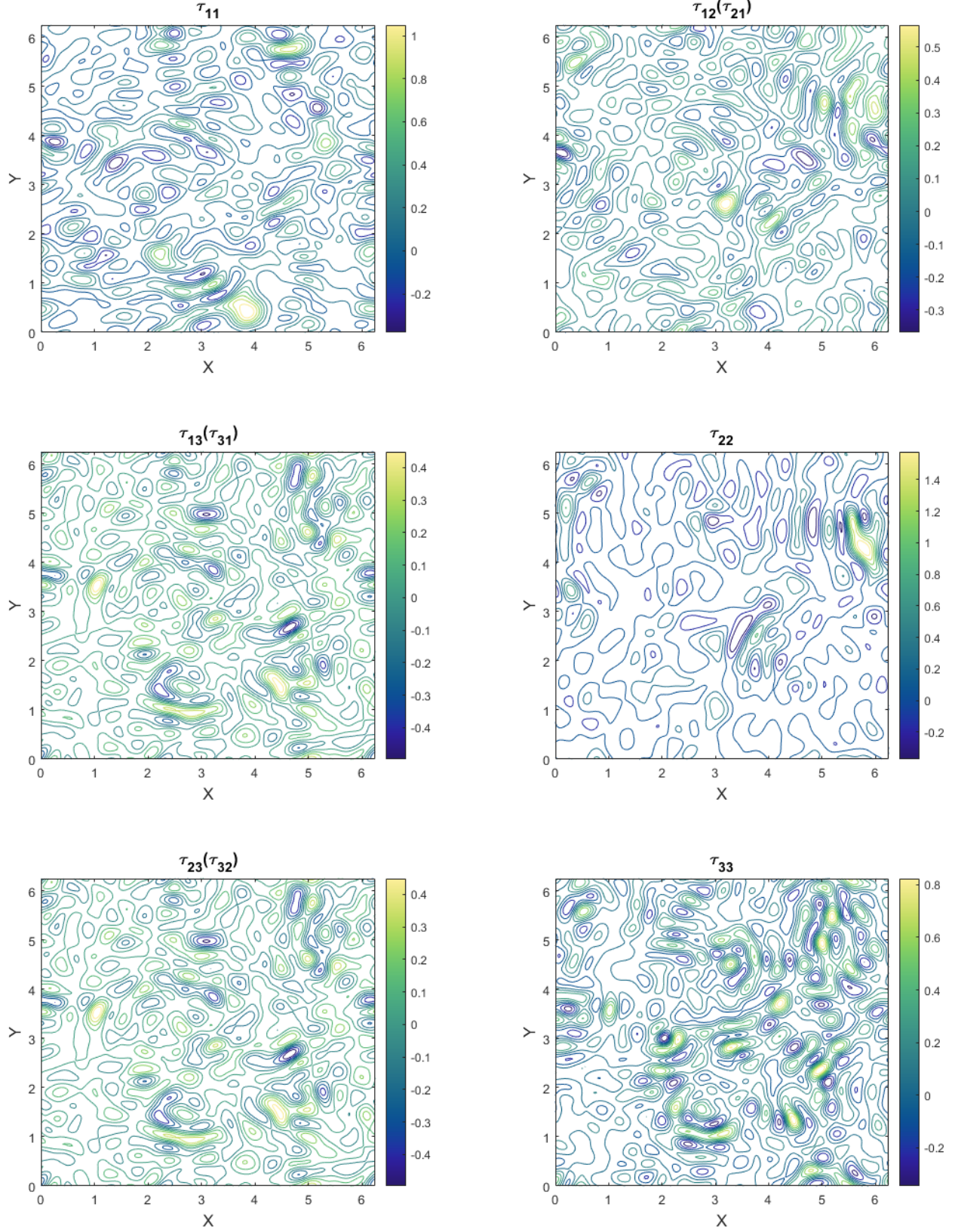


Fig. 16 Bardina's SGS stress tensor τ_{ij} on $x - y$ plane at $z \approx \pi$

References

- [1] Pope, S. B., *Turbulent Flows*, 2013. doi:10.4271/210044.